ACCEPTED MANUSCRIPT
The Journal of Chemical Physics
AIP Publishing
This is the author's peer reviewed, accepted manuscript. However, the online version of record will be different from this version once it has been copyedited and typeset.
PLEASE CITE THIS ARTICLE AS DOI: 10.1063/5.0200042

Rapid Simulation of Two-Dimensional Spectra with Correlated Anisotropic Dimensions

Deepansh J. Srivastava,[1,a)] Jay H. Baltisberger,[2,b)] and Philip J. Grandinetti[3,c)]
[1)] *Hyperfine, Inc., Guilford, CT, USA*
[2)] *Wacker Chemical, Adrian, MI, USA*
[3)] *Department of Chemistry, Ohio State University, 100 West 18th Avenue, Columbus, OH 43210, USA*

A new algorithm has been developed to simulate two-dimensional (2D) spectra with correlated anisotropic frequencies faster and more accurately than previous methods. The technique uses finite-element numerical integration on the sphere and an interpolation scheme based on the Alderman-Solum-Grant algorithm. This method is particularly useful for numerical calculations of joint probability distribution functions involving quantities with a parametric orientation dependence. The technique's efficiency also allows for practical least-squares fitting of experimental 2D solid-state NMR datasets. The simulation method is illustrated for select 2D NMR methods, and a least-squares analysis is demonstrated in the extraction of paramagnetic shift and quadrupolar coupling tensors and their relative orientation from the experimental shifting-d echo ^{2}H NMR spectrum of a $NiCl_2{\cdot}2D_2O$ salt.

I. INTRODUCTION

Numerous multi-dimensional spectroscopic methods have been developed to separate and correlate the anisotropic frequency contributions from tensorial interactions to obtain information about structure and dynamics in solids. In terms of structure, multi-dimensional spectra correlating different tensorial interactions can reveal the principal components of each interaction and the relative orientation between them, providing much stronger structural constraints than isotropic frequencies alone. Examples of such experiments in two-dimensional nuclear magnetic resonance (NMR) include the separation and correlation of anisotropic frequencies of the nuclear magnetic shielding and dipolar coupling[1–4]; nuclear magnetic shielding and first-order quadrupolar coupling[5–9]; nuclear magnetic shielding and second-order quadrupolar coupling[10–13]; and second-order quadrupolar and dipolar coupling[14]. In terms of dynamics, multi-dimensional spectra correlating the same tensorial interaction can reveal the details about motional processes, such as the motional correlation time and the motional mechanism. Examples of such experiments in NMR include the application of 2D exchange methods to polycrystalline solids exploiting the frequency anisotropies arising from the nuclear magnetic shielding[15,16], or the quadrupolar coupling[17–19] tensor.

A primary challenge in using these techniques is the lack of a rapid multi-dimensional simulation algorithm for use in a least-squares analysis of the spectra. Early attempts to circumvent this issue in 2D NMR involved using 2D ridge plots[1] as a visual guide to determining the relative tensor orientations or motional mechanisms. However, ridge plots are not quantitative, and the relative tensor orientations are determined by visual inspection of the spectra. This approach is not only subjective but also time-consuming. A more quantitative process involves using a multi-dimensional simulation algorithm to fit the full experimental multi-dimensional spectrum. This study presents a rapid simulation algorithm for two-dimensional spectra with correlated anisotropic dimensions using finite-element integration. We present the details behind this algorithm and demonstrate its utility, implemented in the Python package *MRSimulator*, in a few illustrative examples of 2D NMR spectroscopy.

[a)] Electronic mail: dsrivastava@hyperfine.io
[b)] Electronic mail: Jay.Baltisberger@wacker.com
[c)] Electronic mail: grandinetti.1@osu.edu

II. ALGORITHM

In 1986, Alderman, Solum, and Grant[20] published an algorithm for rapidly simulating 1D NMR spectra of polycrystalline samples. This approach is based on a finite element integration[21] of the NMR spectrum over the unit sphere. This algorithm, which we refer to as the ASG tenting algorithm, has been widely used for simulating 1D NMR spectra of polycrystalline samples. In this work, we extend the ASG tenting algorithm to 2D NMR spectra having correlated anisotropic dimensions. As the ASG 1D tenting algorithm is part of our 2D algorithm, we present a summary before proceeding with our approach.

A. ASG 1D tenting algorithm

A 1D NMR spectrum of a polycrystalline sample is obtained from the integral

$$\langle s(\nu)\rangle = \int_U \langle s(\nu,\alpha,\beta)\rangle_\gamma \, d\sigma, \tag{1}$$

where U is the unit sphere in $\mathbb{R}^3$ and σ is the solid angle. Here, $\langle s(\nu,\alpha,\beta)\rangle_\gamma$ is the NMR spectrum after an integration over the γ Euler angle,[22] and α and β are the

ACCEPTED MANUSCRIPT
The Journal of Chemical Physics
AIP Publishing
This is the author's peer reviewed, accepted manuscript. However, the online version of record will be different from this version once it has been copyedited and typeset.
PLEASE CITE THIS ARTICLE AS DOI: 10.1063/5.0200042

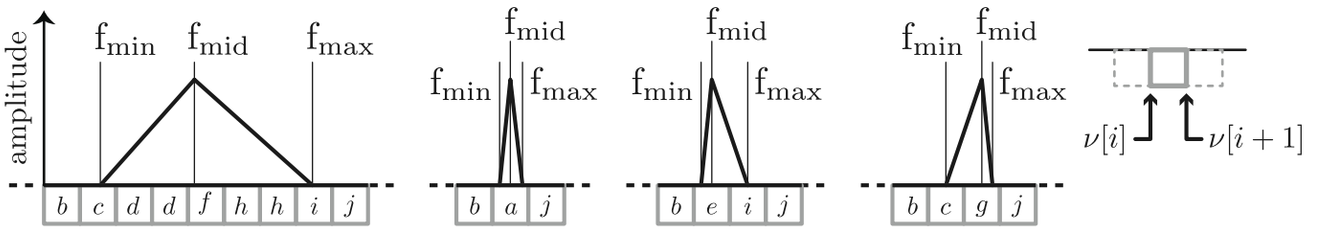

FIG. 1. In the Alderman-Solum-Grant algorithm,[20] the finite-element spectrum obtained after integration over the solid angle of the r^{th} finite element is approximated with a triangular line shape. This figure illustrates the ten bin area cases for "digitizing" the finite-element spectrum in the ASG tenting algorithm as indicated by the letters "a" through "j" in the boxes representing frequency bins below each finite element spectrum. Expressions for the areas of the ten cases are given in reference 20 and the Supplemental Material.

remaining Euler angles. There are numerous situations where a partial average of the NMR signal over the γ angle can be performed analytically,[22] leaving only the 2D integration of α and β to be performed numerically. If the integration over γ cannot be performed analytically, then a separate numerical integration over γ can be performed before or after proceeding with the numerical integration over α and β described here.

Equation (1) can be approximated using finite element integration[21] as

$$\langle s(\nu)\rangle = \sum_{r=1}^{M_\Delta} \int_{\Delta_r} \langle s(\nu,\alpha,\beta)\rangle_\gamma d\sigma = \sum_{r=1}^{M_\Delta} s_{\Delta_r}(\nu), \qquad (2)$$

where $\{\Delta_1,\ldots,\Delta_{M_\Delta}\}$ is a triangulation of U into M_Δ triangles with vertices

$$\begin{aligned}\Delta_r &= \{\vec{e}_{r,A},\vec{e}_{r,B},\vec{e}_{r,C}\}\\ &= \{(\alpha_{r,A},\beta_{r,A}),(\alpha_{r,B},\beta_{r,B}),(\alpha_{r,C},\beta_{r,C})\},\end{aligned} \qquad (3)$$

and $s_{\Delta_r}(\nu)$ is identified as the finite element spectrum obtained after integration over the solid angle of the r^{th} finite element.

There are many algorithms for triangulating the unit sphere. The interpolation method described here can be adapted for any triangular grid mesh on a unit surface. In the ASG orientation sampling algorithm, the triangulation is performed by inscribing an octahedron inside a unit sphere and then subdividing each triangular face of the octahedron into smaller triangles. This triangulation procedure is described in Appendix A. There may be other triangulation schemes that offer faster convergence, but we use the ASG triangulation because it is easy to compute, is scalable, and has an octant symmetry, all of which are useful for a general-purpose NMR simulation.

The frequencies and amplitudes evaluated at the three vertices of a triangle are denoted as (f_A,a_A), (f_B,a_B), (f_C,a_C). In the ASG tenting algorithm, the frequencies are labeled in ascending order and assigned to f_{min}, f_{mid}, and f_{max}, respectively, and the finite element spectrum is approximated as

$$s_{\Delta_r}(\nu) = \left[\frac{w_A a_A + w_B a_B + w_C a_C}{3}\right] \times \text{tri}(\nu,\text{f}_{\text{min}},\text{f}_{\text{mid}},\text{f}_{\text{max}}), \qquad (4)$$

where the w_A, w_B, and w_C are weighting factors. Here, these factors arise from the ASG triangulation described in Appendix A. The function $\text{tri}(\nu,\text{f}_{\text{min}},\text{f}_{\text{mid}},\text{f}_{\text{max}})$ is the normalized triangular distribution function given by

$$\begin{aligned}\text{tri}(\nu,\text{f}_{\text{min}},\text{f}_{\text{mid}},\text{f}_{\text{max}}) &= \frac{2}{(\text{f}_{\text{max}}-\text{f}_{\text{min}})}\\ &\times \begin{cases}(\nu-\text{f}_{\text{min}})/(\text{f}_{\text{mid}}-\text{f}_{\text{min}}), & \text{f}_{\text{min}}\le\nu<\text{f}_{\text{mid}},\\ (\text{f}_{\text{max}}-\nu)/(\text{f}_{\text{max}}-\text{f}_{\text{mid}}), & \text{f}_{\text{mid}}\le\nu<\text{f}_{\text{max}},\\ 0, & \text{otherwise.}\end{cases}\end{aligned} \qquad (5)$$

The triangular line shape assumes that the transition frequencies vary linearly across the triangle's surface and that the differences in amplitude at the vertices are minor. This approximation becomes valid in the limit of large M_Δ.

The i^{th} bin amplitude in the discrete spectrum is obtained by integrating Eq. (5) over the i^{th} bin's frequency interval, i.e.,

$$S_{\Delta_r}[i] = \int_{\nu[i]}^{\nu[i+1]} s_{\Delta_r}(\nu)d\nu. \qquad (6)$$

Here, the limits of the frequency interval of the bin are obtained from

$$\nu[i] = \nu_{\text{low}} + i\Delta\nu, \qquad i = 0,1,\ldots,N_\nu-1, \qquad (7)$$

where ν_{low} is the lower frequency limit of the spectrum, $\Delta\nu$ is the bin interval, and N_ν is the number of bins in the spectrum. Expressions for the areas of ten bin cases, labeled a through j, for "digitizing" the finite-element spectrum in the ASG tenting algorithm are given in reference 20 and the Supplemental Material and are illustrated in Fig. 1.

ACCEPTED MANUSCRIPT
The Journal of Chemical Physics
AIP Publishing
This is the author's peer reviewed, accepted manuscript. However, the online version of record will be different from this version once it has been copyedited and typeset.
PLEASE CITE THIS ARTICLE AS DOI: 10.1063/5.0200042

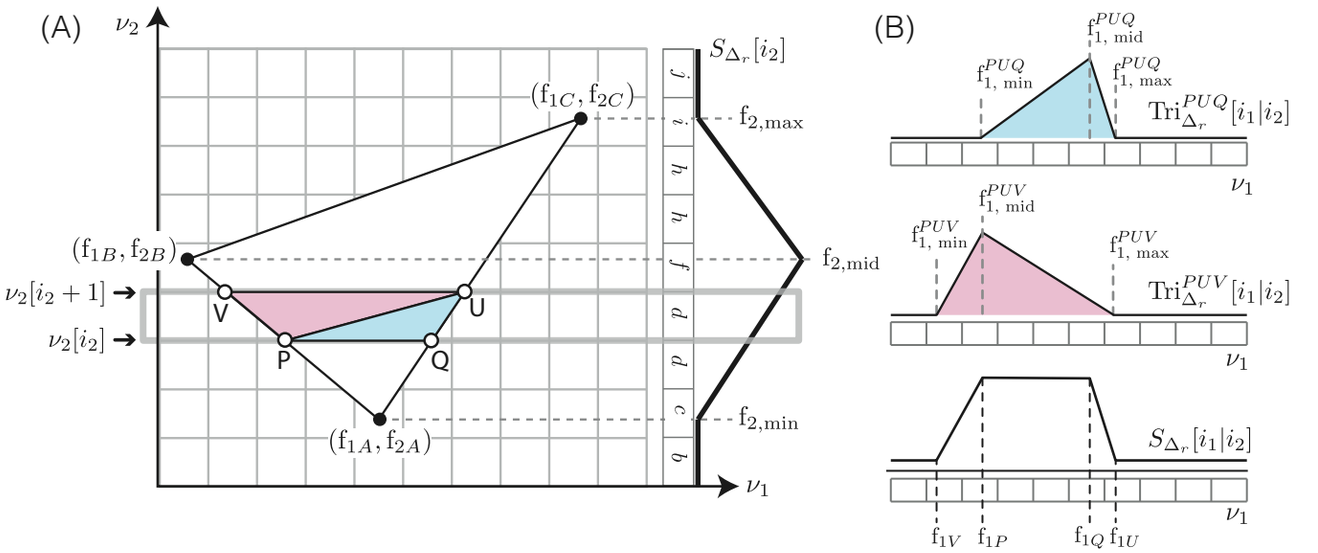

FIG. 2. Illustration of the 2D tenting algorithm. (A) Each cross-section of the 2D finite element spectrum is approximated as the sum of two triangular line shapes whose minimum, middle, and maximum frequencies are obtained from the vertices of two triangles inside the trapezoid, PQUV, as shown above. (B) The relative area of each triangle is distributed into the cross-section bins along the ν_1 dimension using the ASG 1D tenting algorithm. The triangular line shapes obtained from PUV and PUQ are combined using Eq. (18) to obtain the 1D finite element cross-section spectrum. The process is repeated over all bins in ν_2 with non-zero $S_{\Delta_r}[i_1|i_2]$.

B. 2D tenting algorithm

We approximate the 2D spectrum of a polycrystalline sample using a finite-element integration[21] as

$$\langle s(\nu_1,\nu_2)\rangle = \sum_{r=1}^{M_\Delta} \int_{\Delta_r} \langle s(\nu_1,\nu_2,\alpha,\beta)\rangle_\gamma d\sigma = \sum_{r=1}^{M_\Delta} s_{\Delta_r}(\nu_1,\nu_2), \quad (8)$$

where $s_{\Delta_r}(\nu_1,\nu_2)$ is the r^{th} finite-element 2D spectrum obtained after integration over Δ_r. Again, $\langle s(\nu_1,\nu_2,\alpha,\beta)\rangle_\gamma$ is the spectrum after an analytical or numerical partial signal integration over the γ Euler angle.

In the discretization of the 2D spectrum, the $[i_2,i_1]^{\text{th}}$ bin amplitude is obtained by integrating over the i_2^{th} and i_1^{th} bin's frequency intervals, i.e.,

$$S_{\Delta_r}[i_2,i_1] = \int_{\nu_2[i_2]}^{\nu_2[i_2+1]} d\nu_2 \int_{\nu_1[i_1]}^{\nu_1[i_1+1]} d\nu_1\, s_{\Delta_r}(\nu_1,\nu_2), \quad (9)$$

where $(\nu_2[i_2],\nu_2[i_2+1])$ and $(\nu_1[i_1],\nu_1[i_1+1])$ are the lower and upper limits of the corresponding frequency intervals of the 2D bin, and

$$\nu_2[i_2] = \nu_{2,\text{low}} + i_2\Delta\nu_2, \qquad i_2 = 0,1,\ldots,N_{\nu_2}-1, \quad (10)$$

and

$$\nu_1[i_1] = \nu_{1,\text{low}} + i_1\Delta\nu_1, \qquad i_1 = 0,1,\ldots,N_{\nu_1}-1. \quad (11)$$

Here, $\nu_{2,\text{low}}$ and $\nu_{1,\text{low}}$ are the lower frequency limits of the spectrum, $\Delta\nu_2$ and $\Delta\nu_1$ are the bin intervals, and N_{ν_2} and N_{ν_1} are the number of bins along the corresponding dimensions in the spectrum.

In the finite-element integration of a 2D spectrum, the correlated frequency pairs and amplitudes evaluated at the three vertices of a triangle are (f_{1A},f_{2A},a_A), (f_{1B},f_{2B},a_B), (f_{1C},f_{2C},a_C). These three transition frequency coordinates are indicated by the solid black circles in Fig. 2. In our approach, the discretized finite-element 2D spectrum, $S_{\Delta_r}[i_2,i_1]$, is obtained by applying a 1D tenting algorithm to each discretized one-dimensional cross-section of $S_{\Delta_r}[i_2,i_1]$, which is represented as the sum of two triangular line shapes—this approach, illustrated in Fig. 2, proceeds as follows.

The frequencies f_{2A}, f_{2B}, and f_{2C} are sorted in ascending order, and assigned to $f_{2,\text{min}}$, $f_{2,\text{mid}}$, and $f_{2,\text{max}}$, respectively. Using these frequencies, the 1D ASG tenting algorithm is applied to obtain the discretized finite-element spectrum projected onto the ν_2 dimension, i.e., $S_{\Delta_r}[i_2]$, as shown on the right side of Fig. 2A. The amplitude at the i_2^{th} bin of this projection is the integrated amplitude of the corresponding discretized 1D cross-section taken at i_2, i.e., $S_{\Delta_r}[i_1|i_2]$, where

$$S_{\Delta_r}[i_2] = \sum_{i_1=0}^{N_{\nu_1}-1} S_{\Delta_r}[i_1|i_2]\Delta\nu_1. \quad (12)$$

The non-zero amplitude of the discretized 1D cross-section, $S_{\Delta_r}[i_1|i_2]$, is contained inside a trapezoid, PQUV, as shown in Fig. 2A. The coordinates of the

ACCEPTED MANUSCRIPT
The Journal of Chemical Physics
AIP Publishing
This is the author's peer reviewed, accepted manuscript. However, the online version of record will be different from this version once it has been copyedited and typeset.
PLEASE CITE THIS ARTICLE AS DOI: 10.1063/5.0200042

ν_2 bin	P	Q	U	V	$\mathrm{Tri}_{\Delta_r}[i_2]$
a	-	-	-	-	Eq. (S.a)
b	-	-	-	-	Eq. (S.b)
c	$(\mathrm{f}_{1A},\ \mathrm{f}_{2,\mathrm{min}})$	$(\mathrm{f}_{1A},\ \mathrm{f}_{2,\mathrm{min}})$	$(x_{\mathrm{AC}}(y'),\ y')$	$(x_{\mathrm{AB}}(y'),\ y')$	Eq. (S.c)
d	$(x_{\mathrm{AB}}(y),\ y)$	$(x_{\mathrm{AC}}(y),\ y)$	$(x_{\mathrm{AC}}(y'),\ y')$	$(x_{\mathrm{AB}}(y'),\ y')$	Eq. (S.d)
e	$(\mathrm{f}_{1A},\ \mathrm{f}_{2,\mathrm{min}})$	$(\mathrm{f}_{1A},\ \mathrm{f}_{2,\mathrm{min}})$	$(x_{\mathrm{AC}}(\mathrm{f}_{2,\mathrm{mid}}),\ \mathrm{f}_{2,\mathrm{mid}})$	$(\mathrm{f}_{1B},\ \mathrm{f}_{2,\mathrm{mid}})$	Eq. (S.e1)
	$(\mathrm{f}_{1B},\ \mathrm{f}_{2,\mathrm{mid}})$	$(x_{\mathrm{AC}}(\mathrm{f}_{2,\mathrm{mid}}),\ \mathrm{f}_{2,\mathrm{mid}})$	$(x_{\mathrm{AC}}(y'),\ y')$	$(x_{\mathrm{BC}}(y'),\ y')$	Eq. (S.e2)
f	$(x_{\mathrm{AB}}(y),\ y)$	$(x_{\mathrm{AC}}(y),\ y)$	$(x_{\mathrm{AC}}(\mathrm{f}_{2,\mathrm{mid}}),\ \mathrm{f}_{2,\mathrm{mid}})$	$(\mathrm{f}_{1B},\ \mathrm{f}_{2,\mathrm{mid}})$	Eq. (S.f1)
	$(\mathrm{f}_{1B},\ \mathrm{f}_{2,\mathrm{mid}})$	$(x_{\mathrm{AC}}(\mathrm{f}_{2,\mathrm{mid}}),\ \mathrm{f}_{2,\mathrm{mid}})$	$(x_{\mathrm{AC}}(y'),\ y')$	$(x_{\mathrm{BC}}(y'),\ y')$	Eq. (S.f2)
g	$(x_{\mathrm{AB}}(y),\ y)$	$(x_{\mathrm{AC}}(y),\ y)$	$(x_{\mathrm{AC}}(\mathrm{f}_{2,\mathrm{mid}}),\ \mathrm{f}_{2,\mathrm{mid}})$	$(\mathrm{f}_{1B},\ \mathrm{f}_{2,\mathrm{mid}})$	Eq. (S.g1)
	$(\mathrm{f}_{1B},\ \mathrm{f}_{2,\mathrm{mid}})$	$(x_{\mathrm{AC}}(\mathrm{f}_{2,\mathrm{mid}}),\ \mathrm{f}_{2,\mathrm{mid}})$	$(\mathrm{f}_{1C},\ \mathrm{f}_{2,\mathrm{max}})$	$(\mathrm{f}_{1C},\ \mathrm{f}_{2,\mathrm{max}})$	Eq. (S.g2)
h	$(x_{\mathrm{BC}}(y),\ y)$	$(x_{\mathrm{AC}}(y),\ y)$	$(x_{\mathrm{AC}}(y'),\ y')$	$(x_{\mathrm{BC}}(y'),\ y')$	Eq. (S.h)
i	$(x_{\mathrm{BC}}(y),\ y)$	$(x_{\mathrm{AC}}(y),\ y)$	$(\mathrm{f}_{1C},\ \mathrm{f}_{2,\mathrm{max}})$	$(\mathrm{f}_{1C},\ \mathrm{f}_{2,\mathrm{max}})$	Eq. (S.i)
j	-	-	-	-	Eq. (S.j)

TABLE I. Coordinates of trapezoid PQUV and the corresponding integrated amplitude, $S_{\Delta_r}[i_2]$, for the different bin cases in ν_2. Here, $y = \nu_2[i_2]$ and $y' = \nu_2[i_2+1]$. The functions $x_{\mathrm{AC}}(\nu_2)$, $x_{\mathrm{AB}}(\nu_2)$, and $x_{\mathrm{BC}}(\nu_2)$ are given in Eqs. (13-15). The equation numbers tabulated in column $\mathrm{Tri}_{\Delta_r}[i_2]$ refer to the equation number in the Supplemental Material. These are combined using Eq. (18) to obtain the 1D finite element cross-section spectrum. The bin case designations (a to j) are the same as the 1D ASG tenting algorithm shown in Fig. 1 and summarized in the Supplemental Material. The bin cases b and j have zero intensity. The bin case a occurs when $v_2[i_2] \le \mathrm{f}_{2A} \le \mathrm{f}_{2B} \le \mathrm{f}_{2C} \le v_2[i_2+1]$ and 2D interpolation is not required. In this case we proceed with the 1D ASG interpolation on the $(\mathrm{f}_{1A}, \mathrm{f}_{1B}, \mathrm{f}_{1C})$ coordinates.

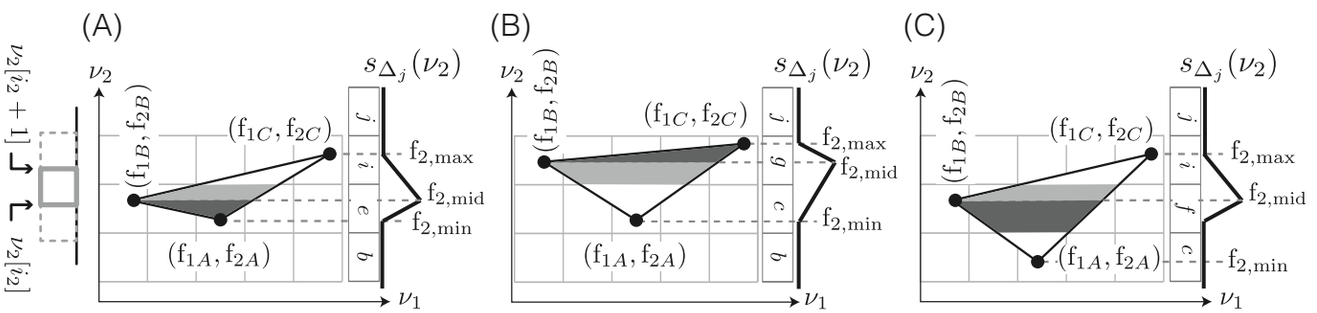

FIG. 3. The figure illustrates the finite-element 2D spectrum for the three bin cases e, f, and g, where the bin intensity is the sum of two trapezoids represented with two different shades of gray.

trapezoid vertices (PQUV) are listed in Table I and are calculated using the equations of lines AB, AC, and BC given by

$$x_{\mathrm{AC}}(\nu_2) = \left(\frac{\mathrm{f}_{1A} - \mathrm{f}_{1C}}{\mathrm{f}_{2,\mathrm{min}} - \mathrm{f}_{2,\mathrm{max}}}\right)(\nu_2 - \mathrm{f}_{2,\mathrm{min}}) + \mathrm{f}_{1A}, \quad (13)$$

$$x_{\mathrm{AB}}(\nu_2) = \left(\frac{\mathrm{f}_{1A} - \mathrm{f}_{1B}}{\mathrm{f}_{2,\mathrm{min}} - \mathrm{f}_{2,\mathrm{mid}}}\right)(\nu_2 - \mathrm{f}_{2,\mathrm{min}}) + \mathrm{f}_{1A}, \quad (14)$$

$$x_{\mathrm{BC}}(\nu_2) = \left(\frac{\mathrm{f}_{1B} - \mathrm{f}_{1C}}{\mathrm{f}_{2,\mathrm{mid}} - \mathrm{f}_{2,\mathrm{max}}}\right)(\nu_2 - \mathrm{f}_{2,\mathrm{mid}}) + \mathrm{f}_{1B}. \quad (15)$$

The 1D cross-section, $S_{\Delta_r}[i_1|i_2]$, is calculated as the sum of two triangular line shapes whose minimum, middle, and maximum frequencies are obtained from two triangles formed from the vertices PUQ and PUV, as shown in Fig. 2A. For the PUQ triangle, the frequencies f_{1P}, f_{1U}, and f_{1Q} are sorted in ascending order, and assigned to $\mathrm{f}_{\mathrm{min}}^{PUQ}$, $\mathrm{f}_{\mathrm{mid}}^{PUQ}$, and $\mathrm{f}_{\mathrm{max}}^{PUQ}$, respectively. Using these frequencies, the PUQ triangle contribution to the discretized 1D cross-section is obtained from

$$\mathrm{Tri}_{\Delta_r}^{PUQ}[i_1|i_2] = \int_{\nu_{1,i_1}}^{\nu_{1,i_1+1}} \mathrm{tri}\left(\nu_1, \mathrm{f}_{\mathrm{min}}^{PUQ}, \mathrm{f}_{\mathrm{mid}}^{PUQ}, \mathrm{f}_{\mathrm{max}}^{PUQ}\right) d\nu_1, \quad (16)$$

as illustrated by the top triangular spectrum in Fig. 2B. For the PUV triangle, the frequencies f_{1P}, f_{1U}, and f_{1V} are sorted in ascending order, and assigned to $\mathrm{f}_{\mathrm{min}}^{PUV}$, $\mathrm{f}_{\mathrm{mid}}^{PUV}$, and $\mathrm{f}_{\mathrm{max}}^{PUV}$, respectively. Using these frequencies, the PUV triangle contribution to the discretized 1D cross-section is obtained from

$$\mathrm{Tri}_{\Delta_r}^{PUV}[i_1|i_2] = \int_{\nu_{1,i_1}}^{\nu_{1,i_1+1}} \mathrm{tri}\left(\nu_1, \mathrm{f}_{\mathrm{min}}^{PUV}, \mathrm{f}_{\mathrm{mid}}^{PUV}, \mathrm{f}_{\mathrm{max}}^{PUV}\right) d\nu_1, \quad (17)$$

as illustrated by the middle triangular spectrum in Fig. 2B. The discretized cross-section of the finite element 2D spectrum is obtained as the area-normalized

ACCEPTED MANUSCRIPT
The Journal of Chemical Physics
AIP Publishing
This is the author's peer reviewed, accepted manuscript. However, the online version of record will be different from this version once it has been copyedited and typeset.
PLEASE CITE THIS ARTICLE AS DOI: 10.1063/5.0200042

weighted sum of the two triangular line shapes, i.e.,

$$S_{\Delta_r}[i_1|i_2] = \frac{S_{\Delta_r}[i_2]}{\mathrm{A_{PUQ}} + \mathrm{A_{PUV}}} \times \left(\mathrm{A_{PUQ}} \cdot \mathrm{Tri}_{\Delta_r}^{PUQ}[i_1|i_2] + \mathrm{A_{PUV}} \cdot \mathrm{Tri}_{\Delta_r}^{PUV}[i_1|i_2]\right), \tag{18}$$

where $S_{\Delta_r}[i_2]$ is the integrated amplitude of the corresponding 1D cross-section taken at $\nu_2[i_2]$, and

$$\mathrm{A_{PUQ}} = \frac{1}{2}\left|(\mathrm{f}_{1P} - \mathrm{f}_{1Q})(\mathrm{f}_{2Q} - \mathrm{f}_{2U})\right|, \tag{19}$$

and

$$\mathrm{A_{PUV}} = \frac{1}{2}\left|(\mathrm{f}_{1V} - \mathrm{f}_{1U})(\mathrm{f}_{2Q} - \mathrm{f}_{2U})\right|, \tag{20}$$

are the area of triangles PUQ and PUV, respectively. This is illustrated by the bottom spectrum in Fig. 2B.

In Table I, the ν_2 bin cases f, e, and g list two trapezoid PQUV vertexes. Here, we perform the interpolation for both trapezoids as described above. The total intensity for the bin is the sum of the two trapezoid intensities. Figure 3 illustrates the two trapezoidal segments for the three ν_2 bin cases. Note that each trapezoid segment is represented as two triangles. In some cases, two vertexes of a trapezoid are identical, in which case, one of the triangles has zero area, and the trapezoid reduces to a triangle.

The previous steps are repeated for each ν_2 bin with a non-zero amplitude in the projection, $S_{\Delta_r}[i_2]$, to obtain the discretized finite-element 2D spectrum, $S_{\Delta_r}[i_1, i_2]$. Finally, a sum of the discretized finite-element 2D spectra, according to Eq. (8), yields the integrated discretized 2D spectrum,

$$\langle S[i_1, i_2]\rangle = \sum_{r=1}^{M_\Delta} S_{\Delta_r}[i_1, i_2]. \tag{21}$$

In closing this section, we note that Charpentier et al.[25] proposed a 2D tenting approach that assumes the projections onto ν_2 and ν_1 are uncorrelated so that the 2D finite element spectrum can be formed by the outer product of the two marginal distributions (projections), i.e.,

$$S_{\Delta_r}[i_1, i_2] = S_{\Delta_r}[i_1] \otimes S_{\Delta_r}[i_2]. \tag{22}$$

This assumption, however, is flawed as the two dimensions of the 2D finite element spectrum are not uncorrelated. Such an approach only yields an accurate 2D spectrum with correlated anisotropic dimensions in the limit of extremely large N_Θ and defeats the advantage of finite element integration. Furthermore, Charpentier et al.[25] never demonstrated this approach on a 2D spectrum correlating anisotropic dimensions.

III. RESULTS AND DISCUSSION

Figure 4 shows a series of simulated ^{13}C-^{1}H separated local field 2D spectra in a polycrystalline sample using the 2D tenting algorithm to correlate the anisotropic frequencies of the nuclear magnetic shielding of the ^{13}C resonance of a carbonyl group with its anisotropic dipolar coupling to ^{1}H for various relative orientations between the dipolar coupling tensor relative to the shielding tensor. Each simulation took only 40 ms on a laptop computer (Apple MacBook Air, 3.49 GHz M2 processor with 8 cores and 24 GB RAM). These spectra were first simulated by Linder et al.[1] for comparison to the experimental ^{13}C-^{1}H separated local field spectrum of ^{13}C-enriched methyl formate acquired at $T = 90$ K. At the time of this work, 1980, Linder et al.[1] could only perform a least-squares analysis on 1D cross-sections taken from the 2D spectrum.

In Fig. 5 are two examples correlating the anisotropic frequencies of the nuclear magnetic shielding to the second-order quadrupolar coupling. In Fig. 5A is a simulation, using the 2D tenting algorithm, of a 2D Switched-Angle Spinning (SAS) spectrum correlating the central transition of $^{87}Rb_2CrO_4$ at 11.7 T at the two rotor angles $(\theta_1, \theta_2) = (70.12°, 54.74°)$. This spectrum was first measured by Shore et al.[10]. A related method, developed by Wang et al.[12] and Ash et al.[13] referred to as COASTER (COrrelation of Anisotropies Separated Through Echo Refocusing), correlates the triple-quantum to central transition frequencies while spinning at a single rotor angle of 70.12°. It has advantages over the SAS method in that the rotor angle is fixed, and the anisotropies of the chemical shift and the quadrupolar coupling can be correlated in orthogonal dimensions, i.e., the "chemical shift" dimension is free from anisotropic quadrupolar interactions, and a "quadrupolar" dimension is free from chemical shift interactions. The simulation of the COASTER spectrum of $^{87}Rb_2CrO_4$ at 9.4 T using the 2D tenting algorithm is presented in Fig. 5B. Each simulations in Fig. 5 took 14 ms on a the same laptop computer. Such 2D measurements of relative tensor orientations can be valuable in structural studies involving half-integer quadrupolar nuclei. For example, in carbonyl-containing systems such as proteins, the ^{17}O quadrupolar-coupling tensor is consistently aligned along the carbonyl bond, but the chemical-shift tensor tends to rotate away from the bond because of substituent effects.[26]

Figure 6 is the final example illustrating correlating the anisotropic frequencies of the paramagnetic shift anisotropy to the first-order quadrupolar coupling of a ^{2}H ($I = 1$) spectrum. Exploiting paramagnetic interactions in NMR spectroscopy has grown immensely in recent decades. This has mainly been through paramagnetic relaxation enhancements and the fermi- and pseudo-contact shifts as structural constraints. An underutilized but equally powerful feature of the paramagnetic interaction is the direct measurement of the resulting NMR shift anisotropy. In contrast to contact

AIP Publishing
The Journal of Chemical Physics
ACCEPTED MANUSCRIPT
This is the author's peer reviewed, accepted manuscript. However, the online version of record will be different from this version once it has been copyedited and typeset.
PLEASE CITE THIS ARTICLE AS DOI: 10.1063/5.0200042

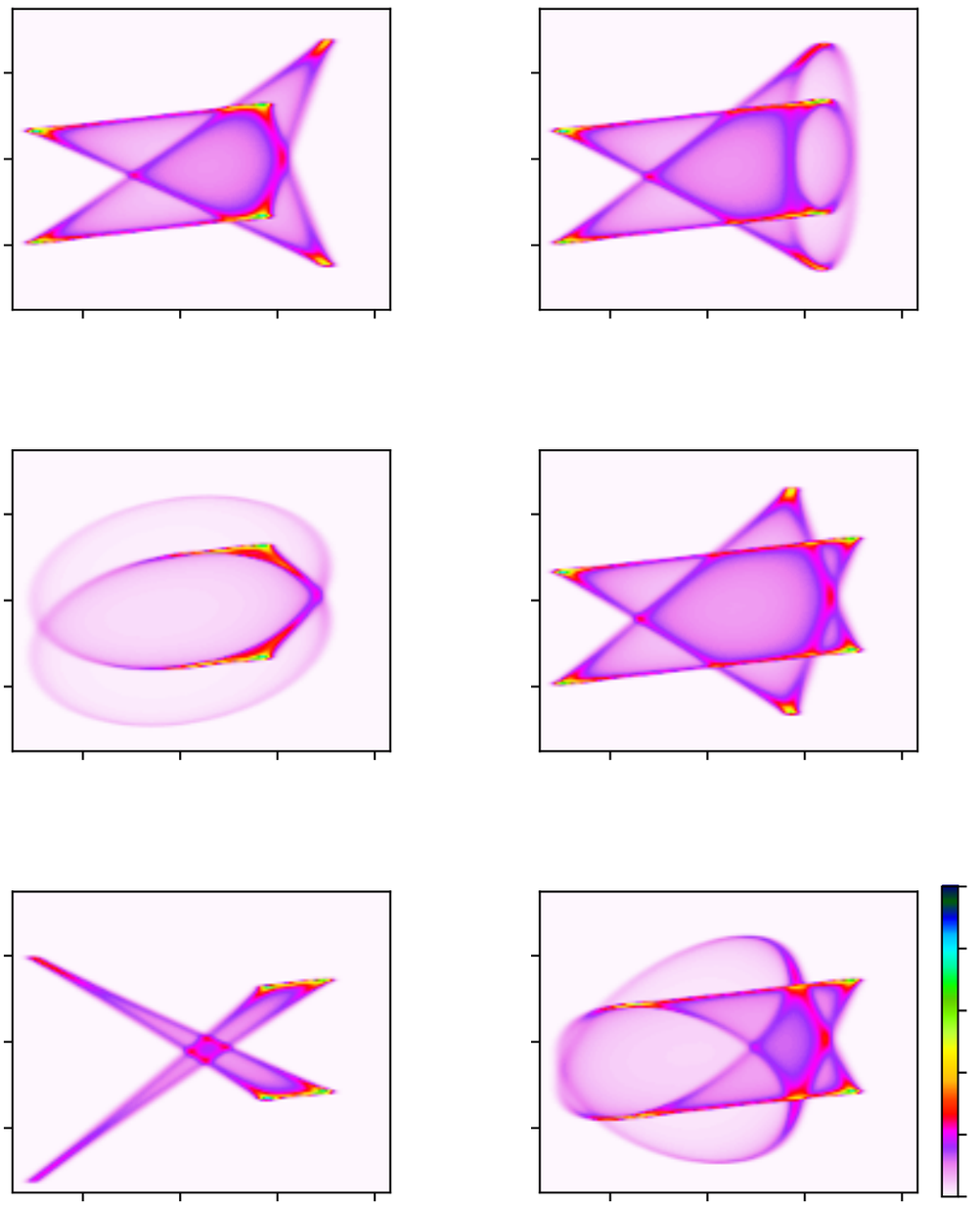

FIG. 4. Simulations using the 2D tenting algorithm of the separated local field spectra of ^{13}C resonance of a carbonyl group with a dipolar coupling to ^{1}H at 2.4 T for various relative orientations between the dipolar coupling tensor and the shielding tensor.[1] The principal components of the chemical shift tensor are $\delta_1 = -126.6$ ppm, $\delta_2 = -7.0$ ppm, and $\delta_3 = 25.4$ ppm for the carbonyl group of methyl formate following the Mehring convention,[23]. The dipolar coupling constant is $\omega_d/(2\pi) = (22\,630/\sqrt{3})$ Hz. The scaling of the dipolar coupling by $1/\sqrt{3}$ is due to the use of Lee-Goldburg decoupling[24] during the t_1 evolution period.[1] Each spectrum is numerically integrated and interpolated over $M_\Delta = 4\,900$ triangular elements, i.e., $\mathfrak{N} = 70$, and took approximately 40 ms on a laptop computer (Apple MacBook Air, 3.49 GHz M2 processor with 8 cores and 24 GB RAM).

ACCEPTED MANUSCRIPT
The Journal of Chemical Physics
AIP Publishing
This is the author's peer reviewed, accepted manuscript. However, the online version of record will be different from this version once it has been copyedited and typeset.
PLEASE CITE THIS ARTICLE AS DOI: 10.1063/5.0200042

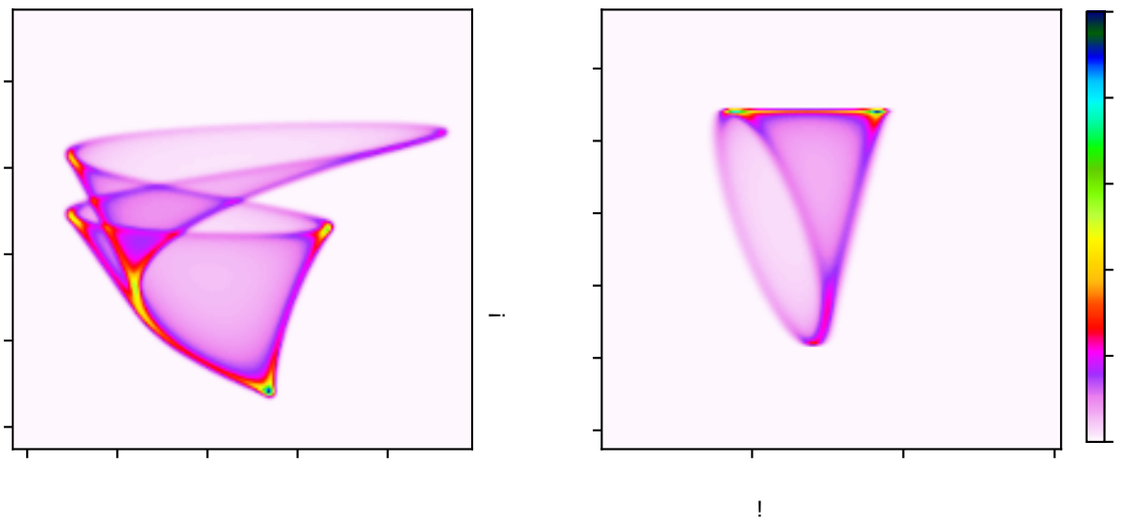

FIG. 5. (A) Simulation using the 2D tenting algorithm of the 2D Switched-Angle Spinning spectrum[10] of $^{87}Rb_2CrO_4$ at 11.7 T correlating the central transition at the two rotor angles $(\theta_1, \theta_2) = (70.12°, 54.74°)$. (B) Simulation using the 2D tenting algorithm of the 2D COASTER[13] spectrum of $^{87}Rb_2CrO_4$ at 9.4 T correlating the triple-quantum to central transition frequencies while spinning at a rotor angle of 70.12°. In both spectra, the ^{87}Rb chemical shift and quadrupolar coupling tensor parameters are $\delta_{iso} = -7$ ppm, $\zeta_\sigma = 110$ ppm, $\eta_\sigma = 0$, $C_q = 3.5$ MHz, $\eta_q = 0.3$, $(\alpha, \beta, \gamma) = (0, 70°, 0)$, following the Haeberlen convention.[23] Each spectrum is numerically integrated and interpolated over $M_\Delta = 4\,900$ triangular elements, i.e., $\mathfrak{N} = 70$, and took approximately 14 ms on a laptop computer (Apple MacBook Air, 3.49 GHz M2 processor with 8 cores and 24 GB RAM).

shifts, which require a high level of computational effort to model, the shift anisotropy can be accurately predicted with a point dipole model.[6,8] Walder et al.[8] used the experimental shifting-d 2D ^{2}H spectrum of a static polycrystalline sample of $NiCl_2{\cdot}2D_2O$ to test hypotheses of different motional models for the water ligands, finding that water ligands coordinated to Ni are located in an unusual pyramidal coordination and undergoing restricted rotations in a concerted motion with neighboring water ligands. Few other techniques can provide this level of detail about the motional dynamics of water ligands—only made possible by stringent constraints from the two-dimensional anisotropic correlation spectra. In Fig. 4B is the simulated shifting-d echo ^{2}H NMR spectrum of the $NiCl_2{\cdot}2D_2O$ salt after a least-squares analysis of experimental 2D spectrum in Fig. 4A using the 2D tenting algorithm. The residuals between the experimental and simulated spectra are shown in Fig. 4C, and the best-fit parameters are given in the caption.

Finally, to quantify the computational efficiency of the 2D tenting algorithm over simply summing spectra from N_Θ orientations without interpolation, we simulated the shifting-d echo ^{2}H NMR spectra as a function of N_Θ with and without the interpolation algorithm. In addition to the ASG orientation sampling scheme (see Appendix A), we included two other schemes in this comparison, ZCW[27] and STEP.[28] The ZCW orientations are generated from solutions of the Diophantine equations,[27,29] and the STEP scheme samples $0 \le \alpha < 2\pi$ and $0 \le \beta \le \pi/2$ on a uniform grid with a weight of $\sin\beta$ each orientation. The triangular grid mesh for the ZCW and STEP coordinates were generated using the Convex hull algorithm.[30] For a visual comparison of the spectra and their corresponding computational times, see section S2 of the supplementary material. For each simulation, a root-mean-square error (RMSE) was calculated between the simulated and a "ground-truth" spectrum obtained from averaging the 2D tent spectra simulated using the ASG, ZCW, and STEP sampling schemes at the highest N_Θ in this comparison (see Fig. 7).

Shown in Fig. 7 is a comparison of the root-mean-square error (RMSE) as a function of N_Θ for 2D spectra simulated without and with the 2D tenting interpolation, respectively. Most importantly, we see that the RMSE of the spectrum is an order of magnitude smaller with interpolation (filled symbols in Fig. 7) compared to no interpolation (open symbols) for all three samplings. Thus, the 2D tenting algorithm requires orders of magnitude fewer orientations to achieve the same level of RMSE. Additionally, we find that there is no significant difference in the convergence rate among the different orienation sampling schemes when using interpolation.

IV. SUMMARY

We present a new algorithm for rapidly performing the powder average integration of 2D spectra of poly-

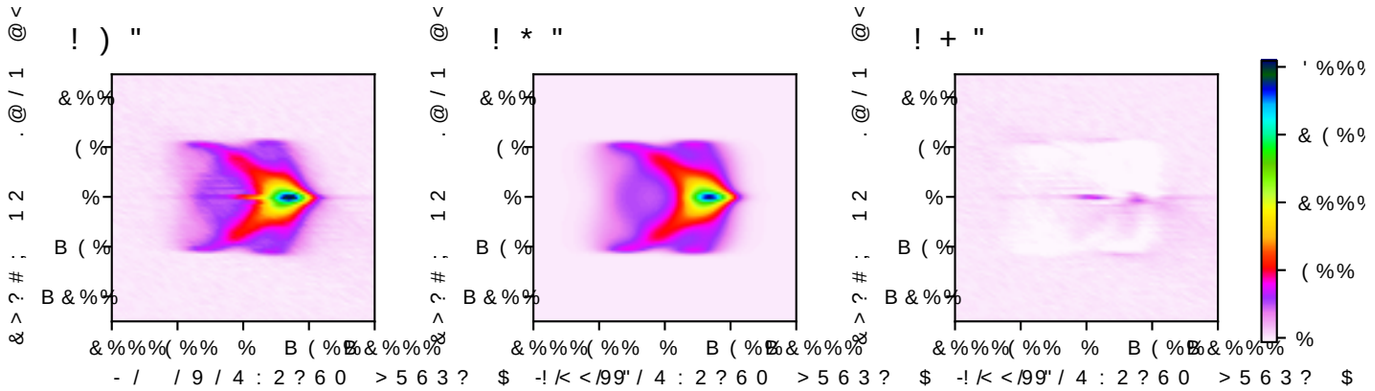

FIG. 6. (A) Experimental shifting-d echo ^{2}H NMR spectrum from the $NiCl_2{\cdot}2D_2O$ salt measured by Walder et al.[8]. (B) Simulation after a least-squares analysis of experimental spectrum in (A) using the 2D tenting algorithm. The paramagnetic shift and quadrupolar coupling tensor best-fit parameters used in the simulation are $\delta_{iso} = -97.1$ ppm, $\zeta_\sigma = -567.6$ ppm, $\eta_\sigma = 0$, $C_q = 75.678$ kHz, $\eta_q = 0.95$, $(\alpha, \beta, \gamma) = (154\,^\circ, 115.7\,^\circ, 180\,^\circ)$, following the Haeberlen convention.[23] More details regarding the determination of parameter uncertainties can be found in Walder et al.[8]. (C) The residuals between the experimental and simulated 2D spectra in (A) and (B). Each spectrum is numerically integrated and interpolated over $M_\Delta = 4\,900$ triangular elements and took approximately 10 ms, and the least-squares analysis of the 2D spectrum took 1.9 s on a laptop computer (Apple MacBook Air, 3.49 GHz M2 processor with 8 cores and 24 GB RAM).

crystalline samples with correlated anisotropic dimensions. The algorithm extends the Alderman-Solum-Grant tenting algorithm for simulating 1D anisotropic spectra of polycrystalline samples to 2D spectra correlating anisotropic dimensions. The convergence of the algorithm is demonstrated to be orders of magnitude faster than simply summing spectra from N_Θ orientations without interpolation, and relatively independent of the orientation sampling scheme.

The algorithm presented here can be extended to multi-dimensional spectra with more than two correlated anisotropic dimensions, although we have neither implemented nor tested it simply because we are unaware of any experimental attempts to measure such spectra–likely due to low sensitivity issues. We expect this situation may improve with future advances in hyperpolarization techniques for solid-state NMR.[31]

The 2D algorithm is implemented in the open-source python package, *MRSimulator*, for simulating NMR spectra of polycrystalline samples with two correlated anisotropic dimensions. The package also includes a least-squares analysis module for fitting experimental spectra to simulated spectra.

SUPPLEMENTARY MATERIAL

Presented in the supplementary material are the amplitude expressions for the ten ASG bin cases, illustrations of convergence with increased triangulation of the sphere and illustrations of various test cases for interpolating 2D triangular segments. Additionaly, Python scripts for simulating Figures 4-7 are provided.

CODE AND DATA AVAILABILITY STATEMENT

The open-source Python package, *MRSimulator*, for implementing the algorithms described here along with documentation for its installation and use, is made available in GitHub at https://github.com/deepanshs/mrsimulator. The documentation for *MRSimulator*, available at https://mrsimulator.readthedocs.io also includes example scripts for obtaining simulations and least-squares analyses of experimental datasets presented in this work, as well as numerous other examples.

ACKNOWLEDGEMENTS

This material is based upon work supported by the Chemical Measurement and Imaging program in the National Science Foundation Division of Chemistry under Grant No. CHE-2107636 (with partial co-funding from the Ceramics program in the Division of Materials Research). P.J.G. also acknowledges support from the Fulbright Scholar Program, sponsored by the U.S. Department of State, the U.S.–Italy Fulbright Commission, and the Centro Risonanze Magnetiche, Universitá degli Studi, Firenze.

ACCEPTED MANUSCRIPT
The Journal of Chemical Physics
AIP Publishing
This is the author's peer reviewed, accepted manuscript. However, the online version of record will be different from this version once it has been copyedited and typeset.
PLEASE CITE THIS ARTICLE AS DOI: 10.1063/5.0200042

ACCEPTED MANUSCRIPT
The Journal of Chemical Physics
AIP Publishing
This is the author's peer reviewed, accepted manuscript. However, the online version of record will be different from this version once it has been copyedited and typeset.
PLEASE CITE THIS ARTICLE AS DOI: 10.1063/5.0200042

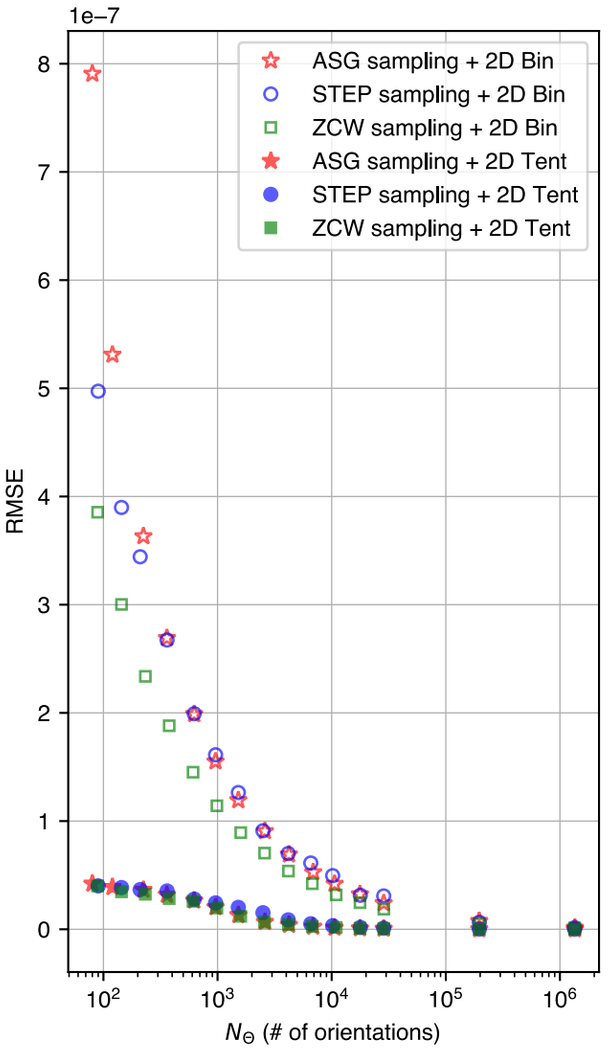

FIG. 7. The root-mean-square error (RMSE) between the simulated and "ground-truth" spectra of the shifting-d echo ^{2}H NMR spectra as a function of N_Θ, the number of orientations used in the powder average. In this comparison, the root-mean-square error (RMSE) is calculated relative to the average 2D tent spectrum obtained using the three sampling schemes with $N_\Theta = 1,352,568$ $1,346,269$ and $1,345,600$ for ASG, ZCW, and STEP sampling, respectively.

ACCEPTED MANUSCRIPT
The Journal of Chemical Physics
AIP Publishing
This is the author's peer reviewed, accepted manuscript. However, the online version of record will be different from this version once it has been copyedited and typeset.
PLEASE CITE THIS ARTICLE AS DOI: 10.1063/5.0200042

Appendix A: ASG Sampling and Triangulation on the Unit Sphere

The ASG sampling and triangulation of the unit sphere can be approximated by first inscribing an octahedron inside a unit sphere. The equilateral triangle faces of the octahedron are further triangulated into $M_\Delta = \mathfrak{N}^2$ equilateral triangles as illustrated in Fig. 3 of the ASG paper[20]. This creates a set of grid intersections (vertices) indexed by k, l, and m, where $0 \leq k, l, m \leq \mathfrak{N}$, and $k + l + m = \mathfrak{N}$. The (x, y, z) coordinates of the grid intersections in the positive octant are given by $(k/\mathfrak{N}, l/\mathfrak{N}, m/\mathfrak{N})$. The distance from the origin to each grid intersection is given by

$$R_{k,l} = \sqrt{x_k^2 + y_l^2 + z_m^2} = \frac{\sqrt{k^2 + l^2 + (\mathfrak{N} - k - l)^2}}{\mathfrak{N}}, \tag{A1}$$

with α and β angles determined by

$$\cos\beta_{l,k} = \frac{\mathfrak{N} - k - l}{\mathfrak{N} R_{l,k}}, \qquad \sin\beta_{l,k} = \frac{\sqrt{k^2 + l^2}}{\mathfrak{N} R_{l,k}}, \tag{A2}$$

and

$$\cos\alpha_{l,k} = \frac{\mathfrak{N} k}{\sqrt{k^2 + l^2}}, \qquad \sin\alpha_{l,k} = \frac{\mathfrak{N} l}{\sqrt{k^2 + l^2}}. \tag{A3}$$

The weight of each orientation, given by

$$w_{l,k} = \frac{1}{R_{l,k}^3}, \tag{A4}$$

accounts for the increase in the area when the planar triangle on the face of the octahedron is extended to the surface of the sphere.

The total number of orientations, N_Θ, is defined as,

$$N_\Theta = \mathcal{F}(\mathfrak{N} + 1)(\mathfrak{N} + 2)/2, \tag{A5}$$

where $\mathcal{F}$ is the number of octant faces.

[1] M. Linder, A. Höhener, and R. R. Ernst, J. Chem. Phys. **73**, 4959 (1980).
[2] T. Nakai, T. Terao, and H. Shirakawa, Chem. Phys. Lett. **145**, 90 (1988).
[3] T. Nakai, J. Ashida, and T. Terao, J. Chem. Phys. **88**, 6049 (1988).
[4] K. Schmidt-Rohr, M. Wilhelm, A. Johansson, and H. W. Spiess, Magn. Reson. Chem. **31**, 352 (1993).
[5] S. Antonijevic and S. Wimperis, J. Chem. Phys. **122**, 044312 (2005).
[6] B. J. Walder, K. K. Dey, M. C. Davis, J. H. Baltisberger, and P. J. Grandinetti, J. Chem. Phys. **142**, 014201 (2015).
[7] T. Iijima and T. Shimizu, Solid State NMR **84**, 234 (2017).
[8] B. Walder, A. Patterson, J. Baltisberger, and P. Grandinetti, J. Chem. Phys. **149**, 084503 (2018).
[9] R. Aleksis, J. P. Carvalho, A. Jaworski, and A. J. Pell, Solid State NMR **101**, 51 (2019).
[10] J. S. Shore, S. H. Wang, R. E. Taylor, A. T. Bell, and A. Pines, J. Chem. Phys. **105**, 9412 (1996).
[11] A. Medek, J. R. Sachleben, P. Beverwyk, and L. Frydman, J. Chem. Phys. , 5374 (1996).
[12] S. H. Wang, Z. Xu, J. H. Baltisberger, L. M. Bull, J. F. Stebbins, and A. Pines, Solid State NMR **8**, 1 (1997).
[13] J. T. Ash, N. T. Trease, and P. J. Grandinetti, J. Am. Chem. Soc. **130**, 10858 (2008).
[14] E. R. H. van Eck and M. E. Smith, J. Chem. Phys. **108**, 5904 (1998).
[15] H. T. Edzes and J. P. C. Bernards, J. Am. Chem. Soc. **106**, 1515 (1984).
[16] P. M. Henrichs and M. Linder, J. Magn. Reson. **58**, 458 (1984).
[17] C. Schmidt, S. Wefing, B. Blümich, and H. Spiess, Chem. Phys. Lett. **130**, 84 (1986).
[18] C. Schmidt, B. Blümich, S. Wefing, S. Kaufmann, and H. W. Spiess, Ber. Bunsenges. Phys. Chem. **91**, 1141 (1987).
[19] C. Schmidt, B. Blümich, and H. Spiess, J. Magn. Reson. **79**, 269 (1988).
[20] D. W. Alderman, M. S. Solum, and D. M. Grant, J. Chem. Phys. **84**, 3717 (1986).
[21] K. Atkinson, J. Austral. Math. Soc. (Series B) **23**, 332–347 (1982).
[22] M. H. Levitt, J. Magn. Reson. **82**, 427 (1989).
[23] R. K. Harris, E. D. Becker, S. M. C. D. Menezes, P. Grangerd, R. E. Hoffman, and K. W. Zilm, Solid State Nucl. Mag. **3**, 41 (2008).
[24] M. Lee and W. I. Goldburg, Phys. Rev. **140**, A1261 (1965).
[25] T. Charpentier, C. Fermon, and J. Virlet, J. Chem. Phys. **109**, 3116 (1998).
[26] G. Wu, K. Yamada, S. Dong, and H. Grondey, J. Am. Chem. Soc. **122**, 4215 (2000).
[27] H. Conroy, J. Chem. Phys. **47**, 5307 (1967).
[28] M. EDÉN, Concepts in Magnetic Resonance Part A **18A**, 24 (2003).
[29] M. Eden and M. H. Levitt, J. Magn. Reson. **132**, 220 (1998).
[30] C. B. Barber, D. P. Dobkin, and H. Huhdanpaa, ACM Transactions on Mathematical Software **22**, 469 (1996).
[31] B. Reif, S. E. Ashbrook, L. Emsley, and M. Hong, Nature Reviews Methods Primers **1** (2021), 10.1038/s43586-020-00002-1.